Identification of the Optic Disk Boundary in Retinal Images using Active Contours

François Mendels[1], Conor Heneghan[2] and Jean-Philippe Thiran[1]

[1]Signal Processing Laboratory (LTS), Swiss Federal Institute of Technology (EPFL),
CH-1015, Lausanne, Switzerland
Tel: 41-21-693-4621 FAX: 41-21-693-7600
mendels@ltssg3.epfl.ch; jp.thiran@epfl.ch
[2]Department of Electronic and Electrical Engineering,
University College Dublin, Belfield, Dublin 4, Ireland
Tel: 706-1925 FAX: 283-0921
conor.heneghan@ucd.ie

Abstract. This paper describes a technique for identifying the boundary of the optic disk in digital images of the retina, using an approach based on active contours (snakes). The optic disk is the region on the retina at which optic nerve axons enter and leave the eye. Changes in optic disk shape and area may indicate disease processes, particularly glaucoma, and accurate identification of the disk boundary may be used to quantify changes. For accurate boundary identification, some pre-processing of the image is necessary. This pre-processing minimises incorrect boundary detection due to blood vessels crossing the optic disk. Pre-processing techniques based on local minima detection and morphological filtering were developed. After pre-processing, the optic disk boundary was determined using an active contour. The contour was driven by a novel external image-derived field called the Gradient Vector Flow. This reduced the need for accurate initialisation of the contour. Results obtained by applying these techniques to a set of nine retinal images are presented.

Keywords: Active Contours, Snakes, Segmentation, Retinal Images, Optic Disk.

1 Introduction

Glaucoma is the second most common cause of blindness in the developed world, accounting for approximately 12.5% of blind registrations [1]. Approximately 1% of the population over 40 will have impaired vision due to glaucoma, and as our population ages, the incidence of glaucoma in the general population will tend to increase. Glaucoma is a disease characterised by elevated intraocular pressure (IOP), which means that the fluid in the eye is at higher pressures than in the normal population. This increased IOP leads to damage of optic-nerve axons at the back of the eye, with eventual deterioration or loss of vision. Optic-nerve axons enter and leave the eye at a site termed the optic disk; a circular structure approximately 2 mm in diameter located at the back of the eye (the fundus). Figure 1 shows a typical monochrome fundus image; the optic disk is the bright circular area in the middle, where the blood vessels converge. This image was obtained using a specially designed medical camera called a fundus camera, that is routinely used by ophthalmologists for assessing the state of the retina and back of the eye. As glaucoma progresses, optic nerve fibres atrophy and changes in the shape and depth of the optic disk are apparent. These changes occur on a slow time scale (years), and quantitative and qualitative comparison of optic disk images over time are a measure of disease progression. Accordingly, accurate image processing techniques for determining the boundary of the optic disk may provide useful clinical information. This paper reports on a technique for finding the outer boundary of the optic disk region using the technique of active contours.

2 Theory

2.1 Overview of Active Contours

In image analysis and computer vision, segmentation is one of the most important steps in allowing successful completion of higher order tasks

such as recognition and tracking. Many techniques have been proposed for segmentation, *e.g.*, globally-based, edge-based, and region-based techniques [2]. An edge-based technique that has been developed in recent years is *active contours*, colloquially known as "snakes" [2,3]. Active contours simulate the fitting of an elastic curve to boundaries or objects of interest in an image. They have been applied to detection of roads and building in remote sensing images [4], feature extraction in faces [5], and 3D segmentation of MRI brain images [6], to name but a few examples.

The active contour model is an energy-minimising contour lying in a damped medium in the plane of an image [2]. The contour is subject to external (image-derived) and internal (contour-based) forces. The contour has the ability to move dynamically in the image space, and can be given inertial properties through the use of an associated mass density m. The medium through which the contour moves is assigned a damping coefficient of g. The final equilibrium position of the contour in the image field will depend upon its initial position and velocity, its mass density and related parameters, the damping coefficient of the space, and external influences due to the image itself (such as lines and edges). Since the contour is a dynamic object, it can converge to arbitrary configurations which correspond to contours of interest in the object, if the external forces and contour parameters are appropriately chosen. Since active contours combine prior knowledge about the object of interest (*i.e.*, smoothness, approximate size), together with individual image characteristics, they provide an excellent framework for detection of the optic disk boundary.

2.2 Mathematical Framework of Active Contours

A grey-scale image I is defined in the x-y image plane, with $I(x,y)$ denoting the value of luminance at position (x,y). The active contour is defined as a parametric time-varying curve $\boldsymbol{v}(s,t)=[x(s,t) \;\; y(s,t)]^T$ in the plane, with s as a normalised parameter representing position on the curve, $s \in [0,1]$, and t as time. [Note: for notational clarity, vectors are written in bold italic throughout this paper]. The contour has a mass density of m and moves in a medium with damping coefficient γ.

An energy functional E_{snake} is associated with this contour, and consists of terms dependent on internal and external influences:

$$E_{snake} = \int_0^1 \left[E_{int}(\mathbf{v}(s,t)) + E_{ext}(\mathbf{v}(s,t)) \right] ds \,, \qquad (1)$$

where $E_{int}(\mathbf{v})$ represents the internal energy of the contour due to kinetic and potential energy terms, and $E_{ext}(\mathbf{v})$ represents energy due to an external energy field generated by the image in which the contour is embedded. The internal energy term can be represented as follows [2,3]:

$$E_{int}(\mathbf{v}) = \frac{1}{2}\left[m\left|\frac{\partial^2 \mathbf{v}}{\partial t^2}\right|^2 + a\left|\frac{\partial \mathbf{v}}{\partial s}\right|^2 + b\left|\frac{\partial^2 \mathbf{v}}{\partial s^2}\right|^2 \right] , \qquad (2)$$

where a quantifies the elasticity of the contour (resistance to stretching), and b determines the rigidity of the snake (resistance to bending). More general formulations are possible in which m, a and b are themselves parameterised by s, but in this paper we assume global fixed values for these coefficients. The first term in Eq. (2) is a kinetic energy term, related to the differential motion of the contour at each point. The second term characterises the potential energy due to stretching of the contour, and is a generalisation of Hooke's law, in which potential energy is proportional to squared extension. The third term represents the potential energy due to bending. In many cases, the mass density of the snake is assumed to be zero so that only the last two terms of Eq. (2) are shown. The external energy E_{ext} represents the effect of forces that are not intrinsic properties of the contour, but which are image dependent. Commonly used definitions of external energy fields include:

$$E_{ext}(x,y) = \begin{cases} E_{ext}^{(1)}(x,y) = -\left|\nabla I(x,y)\right|^2 \\ E_{ext}^{(2)}(x,y) = -\left|\nabla\left[G_s * I(x,y)\right]\right|^2 \end{cases} \qquad (3)$$

where ∇ is the gradient operator, * is the convolution operator, and G_s is a 2D symmetric zero-mean Gaussian function parameterised by s. The first of these external energy fields has minima at places of high image gradient, *e.g.*, edges. The second formulation has minima at

locations where a Gaussian filtered image has maxima, and provides a more diffuse external field. Note that both of these external energy fields are conservative (irrotational), *i.e.*, $\nabla \times \nabla E = 0$.

In this framework, there exists a contour which minimises, at least locally, the energy functional of Eq. (1). Depending on the definition of external force, the location of minimum energy will correspond to a boundary of interest in the image (*e.g.*, it will lie on an edge-defined boundary if $E_{ext}^{(1)}(x, y)$ is used). Returning to Eq. (1), and dropping the dependence on *t*, the energy functional can be recast as a function of $s, \boldsymbol{v}, \frac{d\boldsymbol{v}}{ds}$, and $\frac{d^2\boldsymbol{v}}{ds^2}$:

$$E(\boldsymbol{v}) = \int_{s=0}^{1} F(s, \boldsymbol{v}, \tfrac{\partial \boldsymbol{v}}{\partial s}, \tfrac{\partial^2 \boldsymbol{v}}{\partial s^2}) ds \,. \tag{4}$$

By applying the calculus of variations to this formulation, we obtain the Euler-Lagrange equations that are satisfied when the energy functional is minimised:

$$a \frac{\partial^2 \boldsymbol{v}}{\partial s^2} - b \frac{\partial^4 \boldsymbol{v}}{\partial s^4} - \nabla E_{ext} = 0 \,. \tag{5}$$

Hence, at an energy minimum a force balance exists between internal and external forces:

$$\boldsymbol{F}_{int} + \boldsymbol{F}_{ext} = 0 \,, \tag{6}$$

where

$$\begin{aligned} \boldsymbol{F}_{int} &= a \frac{\partial^2 \boldsymbol{v}}{\partial s^2} - b \frac{\partial^4 \boldsymbol{v}}{\partial s^4} \,. \\ \boldsymbol{F}_{ext} &= -\nabla E_{ext} \end{aligned} \tag{7}$$

The internal forces resist stretching and bending of the contour, while the external force preferentially moves the contour to points of low energy. Since the contour is placed in a medium with a positive damping coefficient, there will be no kinetic energy term at an energy minimum (since motion dissipates energy), so Eqs. (6) and (7) will be satisfied at the final resting place of the contour. A full equation of

motion [3,7] for the contour can be found by adding the inertial and damping terms to Eq. (5) to produce

$$m\frac{\partial^2 \boldsymbol{v}}{\partial t^2}+g\frac{\partial \boldsymbol{v}}{\partial t}+a\frac{\partial^2 \boldsymbol{v}}{\partial s^2}-b\frac{\partial^4 \boldsymbol{v}}{\partial s^4}-\nabla E_{ext}=0, \qquad (\mathbf{8})$$

with initial conditions set by $\boldsymbol{v}(s,0)=\boldsymbol{v}_0(s)$, and all derivatives set to zero, for example. Eq. (8) holds equally for the case of a massless snake (m=0), as implemented in this paper.

2.3 Numerical Solutions for Active Contours

A finite difference method (FDM) can be used for the solution of Eq. (8), under the assumption of zero mass density. We first define a set of N nodes $\mathbf{v}_{i,n}$ of the active contour as:

$$\boldsymbol{v}_{i,n}=\begin{pmatrix} x_{i,n} \\ y_{i,n} \end{pmatrix}=\begin{pmatrix} x[ih] \\ y[ih] \end{pmatrix}_n \qquad (\mathbf{9})$$

with i = 0, 1, …, N-1, h=1/N as a discretisation step for s, and the subscript n indicating evaluation at time step n. The initial conditions are defined as:

$$\boldsymbol{v}_{i,0}=\boldsymbol{k}_i \qquad (\mathbf{10})$$

with $\boldsymbol{k}_i$ as arbitrary initial fixed positions. The last node is constrained to lie next to the first node, so that the contour is closed. The time and space derivatives of Eq. (8) can be approximated by finite differences as:

$$\begin{aligned} &g(\boldsymbol{v}_{i,n}-\boldsymbol{v}_{i,n-1})+a(-\boldsymbol{v}_{i+1,n}+2\boldsymbol{v}_{i,n}-\boldsymbol{v}_{i-1,n})+b(\boldsymbol{v}_{i-2,n}-2\boldsymbol{v}_{i-1,n}+\boldsymbol{v}_{i,n}) \\ &-2b(\boldsymbol{v}_{i-1,n}-2\boldsymbol{v}_{i,n}+\boldsymbol{v}_{i+1,n})+b(\boldsymbol{v}_{i,n}-2\boldsymbol{v}_{i+1,n}+\boldsymbol{v}_{i+2,n})-\begin{pmatrix} f_x(i,n-1) \\ f_y(i,n-1) \end{pmatrix}=0 \end{aligned} \qquad (\mathbf{11})$$

with

$$f_x(i,n-1)=\left.\frac{\partial E_{ext}}{\partial x}\right|_{(x_{i,n-1},y_{i,n-1})} \qquad f_y(i,n-1)=\left.\frac{\partial E_{ext}}{\partial y}\right|_{(x_{i,n-1},y_{i,n-1})} \qquad (\mathbf{12})$$

By arranging the nodes into vectors:

$$\begin{aligned} \boldsymbol{x_n} &= [x_{0,n}, x_{1,n}, \ldots, x_{N-1,n}]^T \\ \boldsymbol{y_n} &= [y_{0,n}, y_{1,n}, \ldots, y_{N-1,n}]^T \end{aligned} \quad (\mathbf{13})$$

a matrix expression for the time evolution of the contour nodes can be written as:

$$\begin{bmatrix} \boldsymbol{x}_n \\ \boldsymbol{y}_n \end{bmatrix} = \begin{bmatrix} (\gamma I + A + B)^{-1} & 0 \\ 0 & (\gamma I + A + B)^{-1} \end{bmatrix} \left\{ \gamma \begin{bmatrix} \boldsymbol{x}_{n-1} \\ \boldsymbol{y}_{n-1} \end{bmatrix} - \begin{bmatrix} \boldsymbol{f}_x(x_{n-1}, y_{n-1}) \\ \boldsymbol{f}_y(x_{n-1}, y_{n-1}) \end{bmatrix} \right\} \quad (\mathbf{14})$$

where the matrices *A* and *B* are tridiagonal and pentadiagonal matrices incorporating the elasticity and stiffness parameters, respectively. This FDM formulation is used to solve numerically for the time evolution of the active contours used in this paper. LU decomposition is used to calculate the matrix inverses efficiently. The stability of this algorithm is not guaranteed [7], and requires numerical experimentation to obtain values of the parameters for which convergence holds.

2.4 Gradient Vector Flow Model

A disadvantage of the active contour model imposed above is that in general there exist many configurations for the snake which are local energy minima, but which do not provide the boundary of interest to us. In general the algorithm will provide a convergent solution that is close to the initial snake configuration; hence, the accuracy of the method is highly sensitive to initialisation. This can be traced back to the fact that a gradient-based external energy field as in Eq. (3) is quite locally defined. If we try to increase the range of the force, by low-pass filtering the image, we lose the ability to obtain an accurate final result. A related problem for snakes defined in this manner is an inability to move into boundary concavities (Figure 1 of [8]). In response to these issues, Xu and Prince proposed a new type of external force field which provides better long range attraction, while preserving sharp local minima in the energy field [8]. Their proposed solution is a static external force field termed the gradient vector flow (GVF) field $F_{ext}^{GVF} = \boldsymbol{h}(x, y)$:

$$F_{ext}^{GVF} = \boldsymbol{h}(x,y) = \begin{pmatrix} p(x,y) \\ q(x,y) \end{pmatrix}. \tag{15}$$

The GVF field $\boldsymbol{h}(x,y)$ is defined to minimise the following energy functional:

$$E_{GVF} = \int_x \int_y \left[l\left(\left|\frac{\partial p}{\partial x}\right|^2 + \left|\frac{\partial p}{\partial y}\right|^2 + \left|\frac{\partial q}{\partial x}\right|^2 + \left|\frac{\partial q}{\partial y}\right|^2 \right) + |\nabla g|^2 |\boldsymbol{h} - \nabla g|^2 \right] dx\, dy, \tag{16}$$

where g is an edge map of the image I, *i.e.* $g(x,y) = \left|\nabla[G_s(x,y) * I(x,y)]\right|$, and λ is a regularisation parameter, which governs the trade-off between the first and second terms in the integrand. The intention is to obtain an extended directional smooth field of attraction, that accounts for the proximity of boundaries, and hence reduces the sensitivity to initialisation. Qualitatively, this formulation is equivalent to the solution of a generalised diffusion equation, and has the effect of increasing the effective range of edges at locations distant from edges. Conversely, near edges, where $|\nabla g|$ is large, the second term is dominant and can be regulated by setting $\boldsymbol{h} \approx \nabla g$ so that the local accuracy is preserved. Again using the calculus of variations, the GVF field can be found by solving the following Euler equations:

$$\begin{cases} l\nabla^2 p - (p - g_x)(g_x^2 + g_y^2) = 0 \\ l\nabla^2 q - (q - g_y)(g_x^2 + g_y^2) = 0 \end{cases} \tag{17}$$

A numerical solution to Eq. (17) can be found by treating p and q as functions of time, and hence converging to a solution. The iterative solution so obtained is fully described in Ref. [8], and convergence of this iterative algorithm is guaranteed for certain values of l. In this paper we use $l = 0.2$ and $N = 80$ iterations for the calculation of the GVF field. After calculation, the GVF field is normalised so that only directional information remains. In this way, the GVF field it is not dependent on overall image luminance levels. A weighted GVF field replaces the original external force field in Eq. (14):

$$k\begin{pmatrix} p^{N}_{x,y} \\ q^{N}_{x,y} \end{pmatrix} = \begin{pmatrix} f_x(x,y) \\ f_y(x,y) \end{pmatrix} \quad \textbf{(18)}$$

with k as an adjustable weight parameter set to 1 in this paper.

2.5 Image Pre-processing

Initial results obtained using the GVF-based snake were quite inaccurate. Figure 1 shows the result for a typical initial condition such as a circle close in radius to the optic disk. The detected boundary is strongly influenced by strong edges created by blood vessels crossing the optic disk. Other initialisations also lead to incorrect results.

Fig. 1. Convergent solution of a GVF-based snake for a simple initialisation condition (smooth inner circle). The boundary found does not correspond to the true edge of the optic disk region, as the snake has been influenced by the edges created by blood vessels.

These erroneous results occur because the GVF field is based on an edge map calculated from the raw image, in which blood vessels make a major contributions to edges. To obtain correct convergence onto the boundary of the optic disk, we need to pre-process the image to remove pixels corresponding to vascular structures, and replace them by pixels representative of the optic disk background behind. Two different methods of pre-processing are used in this paper – minima detection and morphological filtering.

Minima detection makes use of the observation that the luminance of a vessel pixel is darker than the surrounding optic disk. Accordingly we

pass through the region of interest containing the optic disk and compare the luminance level of points in a local neighbourhood. This comparison proceeds as follows. For each point $I(k,l)$ we select sets of surrounding points in the shape of two crosses at 45^{o} relative to one another. The crosses extend to $\pm x$ pixels in all directions. If the luminance of the centre point is less than 90% of the luminance of all of the extrema on the crosses, then it is marked as a candidate vessel pixel. This process is carried out for x=1, 2, 3, and 4. The first pass through the image results in a large set of candidate pixel points, many of which are spurious. Since vessels are connected structures, we make use of this fact by performing successive erosions and dilations using a set of four simple 3x3 structuring elements:

$$F_1 = \begin{bmatrix} 1 & 0 & 0 \\ 0 & 1 & 0 \\ 0 & 0 & 1 \end{bmatrix} \quad F_1 = \begin{bmatrix} 0 & 1 & 0 \\ 0 & 1 & 0 \\ 0 & 1 & 0 \end{bmatrix}$$
$$F_3 = \begin{bmatrix} 0 & 0 & 1 \\ 0 & 1 & 0 \\ 1 & 0 & 0 \end{bmatrix} \quad F_4 = \begin{bmatrix} 0 & 0 & 0 \\ 1 & 1 & 1 \\ 0 & 0 & 0 \end{bmatrix} \qquad (\mathbf{19})$$

Nearby vessel pixels may still be disconnected, so this step is followed by restoration of pixels which share common 4-connected neighbours. These processes result in a collection of pixels which are classed as vessel pixels. They are now replaced by “average” optic disk pixels calculated by taking an average value over the local neighbourhood excluding vessel pixels. Improved results were obtained by first using an unsharp mask on the image, prior to minima detection.

A completely morphological technique for pre-processing was also devised. For typical images, vessel widths do not exceed 5 pixels in diameter. Accordingly, we increase the luminance level of vessel pixels by applying a grey scale dilation with a 5x5 structuring element of constant value. Since this tends to alter the position of the optic disk boundary, the dilation is followed by an erosion using the same structuring element to restore the boundary to its original position. Finally, we perform a morphological reconstruction by retaining the maximum of the dilated/eroded image and the original. We used slightly different definitions to those normally encountered as our aim

was to remove darker areas from the image. Specifically, we used the following definitions of dilation, erosion, and reconstruction:

Dilation :

$$(I \oplus G)(x,y) = \min_{(z_x,z_y)\in G,\,(x-z_x,y-z_y)\in I} \{I(x-z_x, y-z_y) + \bar{I}(x-z_x, y-z_y).G(z_x,z_y)\},$$

Erosion :

$$(I \ominus G)(x,y) = \max_{(z_x,z_y)\in G,\,(x-z_x,y-z_y)\in I} \{I(x+z_x, y+z_y) + \bar{I}(x+z_x, y+z_y).G(z_x,z_y)\}, \quad \textbf{(20)}$$

Reconstruction :

$$I_{rec} = \max\{I(x,y), ((I \oplus G) \ominus G)\},$$

with the overbar denoting averaging, and the dot indicating element-by-element multiplication. These morphological operations result in a 'filling-in' of the vascular structure, by pixels from the surrounding optic disk area. A schematic of these three processing steps is given in Figure 2 for a cross-sectional slice through the image.

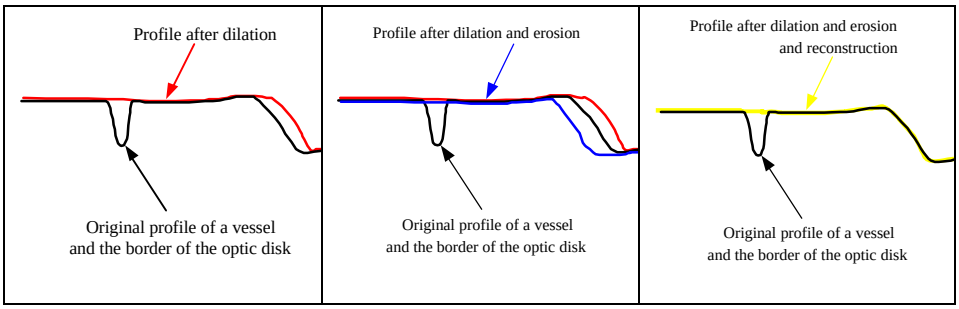

Fig. 2. Representation of the three stages of morphological filtering which are used for pre-processing.

3 Results

The techniques described above were applied to a set of nine retinal images taken from the Digital Library of Ophthalmology at The New York Eye and Ear Infirmary (http://www.nyee.edu). These images were originally acquired as 35 mm slides using a Nikon colour fundus camera. Images were scanned into digital format using a slide scanner. The images analysed in this study were processed at a resolution of 285 x 400 pixels The colour images were initially stored in RGB format,

but were converted to the YIQ basis prior to processing. Thereafter, the images were processed in the luminance (Y) domain. The results of the pre-processing algorithm are shown in Figure 3. Figure 3(a) shows the result when the minima detection scheme was used to pre-process the image; Figure 3(b) shows the result when the morphological correction technique was used. Both techniques are successful in removing the presence of vessels in the optic disk region. However, the minima detection scheme leaves traces of the original vascular structure, whereas the morphological technique totally removes all traces of the vascular structure. Both techniques leave the boundary of the optic disk region intact.

A GVF field was calculated based on the resultant image. The first stage in its calculation is the production of an edge map, typically taken as a binary map. The edge map was calculated using the Marr-Hildreth operator (Laplacian of Gaussian). This edge detector detects zero crossings of the second derivative of the image. The Marr-Hildreth operator is parameterised by s, the width of a 2D Gaussian filter which reduces noise sensitivity. To provide an improved edge map, we combined the results of three binary edge maps**,** to get weighted edges, using s =1.5, 2.0, and 2.5 (corresponding respectively to 11 x 11, 13 x 13, and 17 x 17 convolution masks). The threshold for each individual edge map is set as a function of s, leading to an edge map with values 0,1/3, 2/3, 1. The GVF field is then found by applying the iterative algorithm described earlier. The regularisation parameter λ is chosen to be 0.2. After the GVF field is calculated, it is normalised, so that only the directional information remains. The active contour was then interactively initialised by choosing approximately 10 points close to the contour of interest. These 10 points were linearly extrapolated to form a set of nodes evenly spaced by some maximum distance (*e.g.*, 3 pixels). Typically, this gave a set of approximately 100 nodes. The contour was chosen to have an initial velocity of zero. The parameters for the contour and medium were set to a=2, b=1.5, and γ=2. These values were determined empirically by numerical experimentation. Values of a and b equal to or close to zero lead to sharp corners, discontinuities, crossovers, and loopbacks which are undesirable. Too high a value of these parameters means that the snake is overly constrained in size and smoothness.

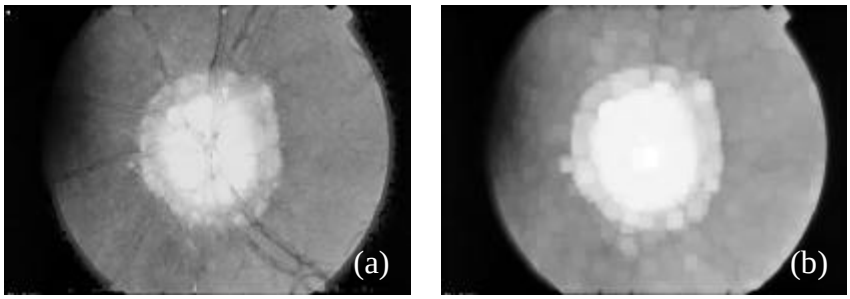

Fig. 3. (a) . Image pre-processed using the minima detection method described in text. (b) Same image pre-processed using the morphological technique described in text.

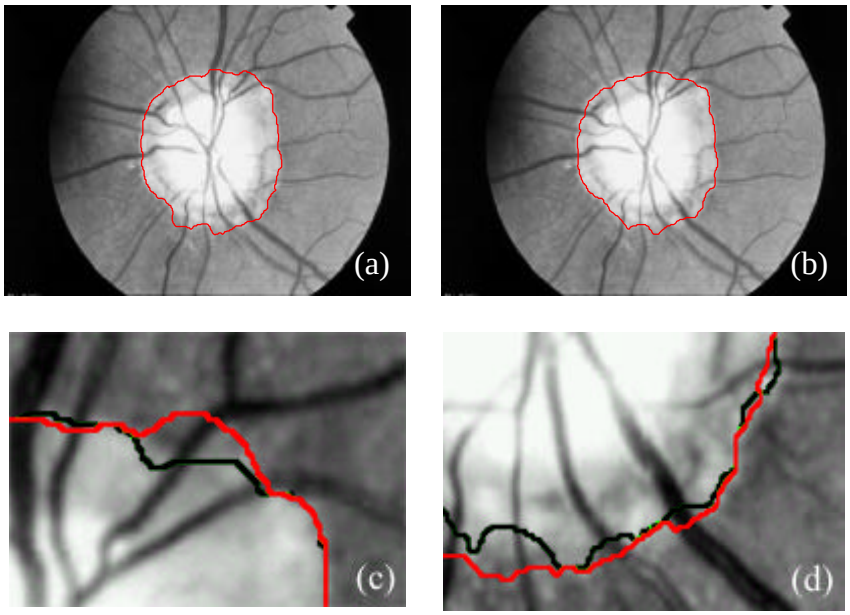

Fig. 4. Boundaries detected using the GVF active contour applied to the preprocessed images. (a) Boundary extracted based on the image which has been pre-processed using minima detection (b) Boundary extracted based on the image which has been pre-processed using morphological filtering (c) Close-up of the minor differences between the detected boundaries on the upper optic disk edge (dark curve corresponds to morphological pre-processing, mid grey to minima detected pre-processing). (d) Minor differences between the detected boundaries on the lower optic disk edge.

The numerical algorithm of Eq. (14) typically provided convergent results after approximately 50-200 iterations (depending on the

proximity of the initial conditions to the final boundary). The results shown here are for 200 iterations. Figures 4(a) and (b) show the boundaries determined for an image that had been pre-processed by the minima detection and morphological schemes, respectively. Figures 4(c) and 4(d) shows detailed views of minor differences between the determined boundaries. Both pre-processing techniques lead to accurately detected boundaries; however, in this example the result for the morphologically pre-processed image is qualitatively better.

4. Conclusions and Discussion

The results indicate that a GVF-based snake can be used in conjunction with a pre-processed fundus image to extract an accurate boundary for the optic disk region. Pre-processing is an essential step for accurate convergence, and will be needed for any general problem which requires boundary detection in the presence of small occluding objects. An attractive feature of the GVF contour, as compared to previous active contour techniques is its relative insensitivity to initial conditions. Prior to using the GVF model, we investigated more usual snake formulations based on the image gradient as an external field, but achieved results which were highly dependent on initial conditions. For the GVF snake, we conducted initial studies of the range of initialisation conditions that provide convergence, and found that accurate solutions can be obtained from quite distant initial conditions (*e.g.*, circles ranging from approximately half to double the radius of the optic disk.) It is also possible to use initial conditions which traverse the final boundary repeatedly. Robust convergence across a large range of initial conditions is important if fully automated image analysis is desired, where a simple initialisation scheme will be needed.

The sensitivity of this technique to image variations was also considered. There are two potential sources of variation. In some images, the optic disk boundary is not well defined, due to either natural variation or pathological changes. Variations can also be introduced by photographic conditions, *e.g.*, too little or too much light, poor image contrast, *etc*. In the nine images considered, an accurate convergent boundary was found in all cases, even those with quite severe retinal pathologies. Overall, morphological pre-processing

provided better solutions that were the least sensitive to initial conditions, and which captured subtle details of the disk boundary.

Three clinical ophthalmologists have reviewed the boundaries extracted by this technique, and consider it as a promising technique for clinical use. However, a much more systematic evaluation of the technique is now required. Specifically, the technique will be applied to a set of images of known clinical aetiology. Optic disk parameters for disk area and boundary length will be evaluated, to see if quantitative evaluation of these parameters correspond with clinical findings.

The technique may also form part of a more general image analysis scheme for fundus images. Automated analysis of fundus images requires segmentation of the image into regions such as optic disk, fovea, vessels, and background retina. The scheme described here can form part of this segmentation process. Moreover, the morphological pre-processing scheme is a useful technique for extracting the vasculature, an area of current research by other investigators [9].

References

1. World Health Organization (WHO) Publication PBL/87.14 (Update 1987), Available Data on Blindness. WHO, Geneva, Switzerland, 1987.
2. Sonka, M., Hlavac, V.,. Boyle, R.: Image Processing, Analysis and Machine
3. Kass, M., Witkin, A., Terzopoulos, D.: Snakes: Active Contour Models, Int. J. Computer Vision, 1 (1987), 321–331.
4. Fua, P., Leclerc, Y. G.: Model driven edge detection. In Proceedings of the Image Understanding Workshop, Cambridge, MA (1988), 1016–1021.
5. Yuille, A. L., Cohen, D. S., Hallinan, P. W.: Feature extraction from faces using deformable templates. In Computer Vision and Pattern Recognition, San Diego, CA (1989), 104–109.
6. Cohen, L. D., Cohen I.: Finite Element Methods for Active Contour Models and Balloons for 2D and 3D Images, IEEE Trans. Patt. Anal. Mach. Intell., 15 (1993), 1131–1147
7. Samadini, R.: Adaptive Snakes: Control of Damping and Material Parameters, SPIE vol. 1570, Geometric Methods in Computer Vision (1991), 202–213.
8. Xu., C. and Prince, J.L.: Snakes, Shapes, and Gradient Vector Flow, IEEE Trans. Image Processing, 1 (1998), 359–369.
9. Matsopoulos, G. K., Mouravliansky, N. A., Delibasis, K. K., Nikita, K. S.: Automatic Retinal Image Registration Scheme using Global Optimization Techniques. IEEE Trans. Info. Tech. Biomed. 3 (1999), 47–60.